

Modeling of screening currents in coated conductor magnets containing up to 40000 turns*

Enric Pardo

Institute of Electrical Engineering, Slovak Academy of Sciences,
Dubravska 9, 84104 Bratislava, Slovakia
enric.pardo@savba.sk

March 4, 2024

Abstract

Screening currents caused by varying magnetic fields degrade the homogeneity and stability of the magnetic fields created by *REBCO* coated conductor coils. They are responsible for the AC loss, which is also important for other power applications containing windings. Since real magnets contain coils exceeding 10000 turns, accurate modeling tools for this number of turns are necessary for magnet design. This article presents a fast numerical method to model coils with no loss of accuracy. We model a 10400-turn coil for its real geometry and coils of up to 40000 turns with the continuous approximation, which we checked that introduces negligible errors. The screening currents, the Screening Current Induced Field (SCIF) and the AC loss is analyzed in detail. The SCIF is maximum at the remnant state with a considerably large value and decreases substantially after one day of relaxation. The instantaneous AC loss for an anisotropic magnetic-field dependent J_c is qualitatively different than for a constant J_c , although the loss per cycle is similar. Saturation of the magnetization currents at the end pancakes causes that the maximum AC loss at the first ramp increases with J_c . The presented modeling tool can accurately calculate the SCIF and AC loss in practical computing times for coils with any number of turns used in real windings, enabling parameter optimization.

1 Introduction

Time varying magnetic fields create screening currents in superconductors [1]. The screening currents induced at the charge and discharge ramps of magnets distort the generated magnetic field [2], being this critical for magnet applications like Magnetic Resonance Imaging (MRI), Nuclear Magnetic Resonance (NMR) and accelerator magnets. In addition, screening currents create dissipation in the winding, which increases the running costs and complicates the

*The final version of the article can be found in the publication only: *Supercond. Sci. Technol.*, vol. 29, a.n. 085004 (2016), <http://dx.doi.org/10.1088/0953-2048/29/8/085004>.

cryogenics. This is also relevant for other applications containing windings, such as Superconducting Magnetic Energy Storage (SMES), transformers and rotating machines. Screening currents in *REBCO*¹ coated conductors, with relatively high width, are of higher importance than in multi-filamentary wires, such as NbTi, Nb₃Sn or MgB₂. In addition, superconducting magnets (and SMES) may contain thousands of turns [3, 4], reaching up to around 30000 turns [5]. Therefore, modelling of the screening currents in superconducting windings of high number of turns is necessary for the design of these applications.

The interaction between screening currents strongly impact their magnitude, as has been found for stacks of tapes in external applied magnetic field [6–8] and coils [9, 10]. Modelling of the screening currents taking their interaction between all turns into account have been published for pancake coils (or pancakes) with more than 100 turns [11–14] and stacks of pancakes with up to 768 turns [15, 16]. In order to model higher number of turns with practically no loss in accuracy, the continuous approximation has been developed [9, 12, 17]. This allowed to model coils of up to 4000 turns [18–21]. Predecessor models of the continuous approximation have been published in [22, 23], which take additional approximations. Semi-analytical models have also been applied to model magnet size coils with up to around 30000 turns, under certain approximations [24]. Coils of around 900 turns have been modeled by a 3D numerical method, which intrinsically assumes the thin film geometry of the tapes [25].

This work presents a method to accurately calculate the screening currents in coils containing more than 10000 turns (one order of magnitude higher than previous works) with feasible computing times². By means of the continuous approximation, the number of turns is extended up to 40000. This fulfills the present requirements for high-field magnets and other applications containing windings. When using the real geometry, the numerical method does not assume that the tape is a thin film; and hence current penetration across the thickness can be modeled, which is important for coils made of powder-in-tube tapes like Bi2223.

By means of this method, we calculate the Screening Current Induced Field (SCIF) at the center of a 10400-turn coil for both a cyclic ramp-up and ramp-down process and relaxation after the end of the first ramp down, or remnant state. The article also presents the SCIF at the remnant state for coils from 800 to 40000 turns. We analyze in detail the instantaneous AC loss in the 10400 turn coil for cyclic ramp-up and ramp-down. Although this work regards the coil as a stand-alone magnet, adding the effect of the magnetic field generated by an outsert is straightforward.

2 Studied geometry

This article analyzes in detail the winding with parameters in table 1, which contains 10400 turns and its cross-section is in figure 1. In section 4.2.3, We also present the Screening Current Induced Field (SCIF) at the remnant state and the critical current for coils with the same parameters as in table 1 but 2

¹*REBCO* stands for *REBa₂Cu₄O_{7-x}*, where *RE* is a rare earth, usually Y, Gd or Sm.

²The essence of the numerical model in this article and part of the results have been presented in conferences between 2014 and 2015 [26, 27]; presentations are available on-line in [26, 28].

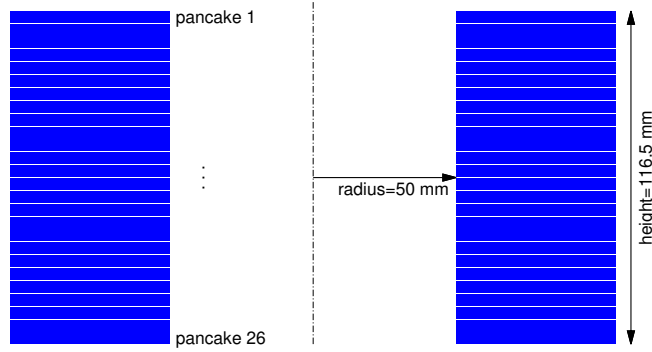


Figure 1: Sketch of the cross-section of the coil of the main analysis, containing 10400 turns. Computations for other coils only differ in the total number of pancakes.

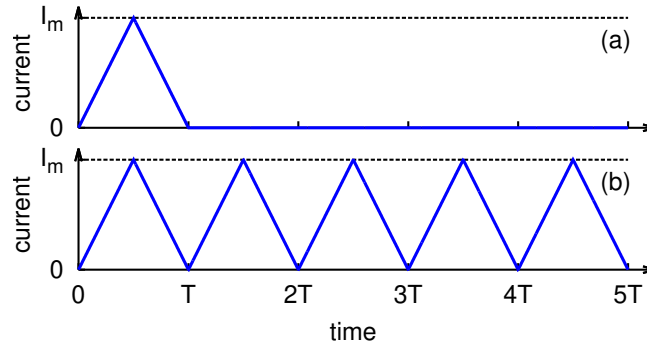


Figure 2: Qualitative time signal of the current for (a) remnant state relaxation and (b) cyclic excitation.

number of pancakes	26
number of turns per pancake	400
total number of turns	10400
inner radius	50 mm
outer radius	105.9 mm
superconducting layer thickness	2 μm
superconducting layer width	4 mm
radial separation between superconducting layers	138 μm
axial separation between pancakes	0.5 mm

Table 1: Parameters of the coil of the main analysis. Calculations for other coils only differ in the total number of pancakes.

to 100 pancakes (800 to 40000 turns).

3 Model

We calculate the screening currents by means of the Minimum Magnetic Entropy Production (MEMEP) method [18]. This numerical method computes the detailed current density in each turn for any given $E(J)$ relation, where E and J are the electric field and current density, respectively. In axially symmetric geometries, J is the angular component of the current density. In this article, we assume

$$E(J) = E_c \left(\frac{|J|}{J_c} \right)^n \frac{J}{|J|}, \quad (1)$$

where J_c is the critical current density, n is the power-law exponent and $E_c = 10^{-4}$ V/m. We took the dependence of J_c on the magnetic field³ B and its angle with the normal of the tape surface θ from [29], based on fitting experiments of a 4 mm wide SuperPower tape [30] at 4.2 K from self-field to 30 T. Using the angle θ definition of figure 3, the fit for the tape critical current in [29] is

$$I_{ct}(B, \theta) = \frac{K_0}{\left(\frac{B}{\beta_0} + 1\right)^{a_0}} + \frac{K_1}{\left(\frac{B}{\beta_1} + 1\right)^{a_1}} \cdot [\omega^2(B) \cos^2(\theta - \theta_0) + \sin^2(\theta - \theta_0)]^{-1/2} \quad (2)$$

with

$$\omega(B) = \left(\frac{B}{\beta_\omega} + 1 \right)^{5/3} \quad (3)$$

where B is the applied magnetic field and we re-wrote the equations above in order to get constants with integer dimensions, with values $K_0 = 292.5$ A, $K_1 = 2213$ A, $\beta_0 = 13.8$ T, $\beta_1 = 13.8$ T, $\beta_\omega = 0.2792$ T, $a_0 = 1.3$, $a_1 = 0.809$ and $\theta_0 = -0.180^\circ$. At high magnetic fields, this $I_{ct}(B, \theta)$ dependence presents a sharp peak at $\theta = 90.18^\circ$ and a wide plateau around $\theta = 0^\circ$ (figure 3). In this article, we assume that $J_c(B, \theta) = I_{ct}(B, \theta)/(wd)$, where we take B as the local magnetic field and w is the tape width and d is the thickness of the superconducting layer. Then, we assume that the tape self-field is negligible compared to the total magnetic field in the magnet, at least in the regions where J is limited by J_c .

The main improvement in the numerical method from [18] is an iterative process to reduce the computing time, while obtaining accurate results of the screening currents. We divide the coil cross-section in sectors containing several turns (figure 4), where the width of each sector in the radial direction is as close as possible to the tape width (except the last sector in each pancake, which contains the remaining tapes). The tapes in the sectors are divided into elements, where J is assumed uniform. We start at the initial time t_0 with a known solution of the current density, J_0 , for a given current I_0 . After increasing the time by Δt , the routine calculates the change in current density ΔJ due to the change in current ΔI (note that $t = t_0 + \Delta t$, $J = J_0 + \Delta J$ and $I = I_0 + \Delta I$). The algorithm to obtain ΔJ is outlined in figure 5. First, the

³In this article we refer to the magnetic field (or “field”), \mathbf{H} , and magnetic flux density, \mathbf{B} , indistinctly because magnetic materials are not present, and hence $\mathbf{B} = \mu_0 \mathbf{H}$.

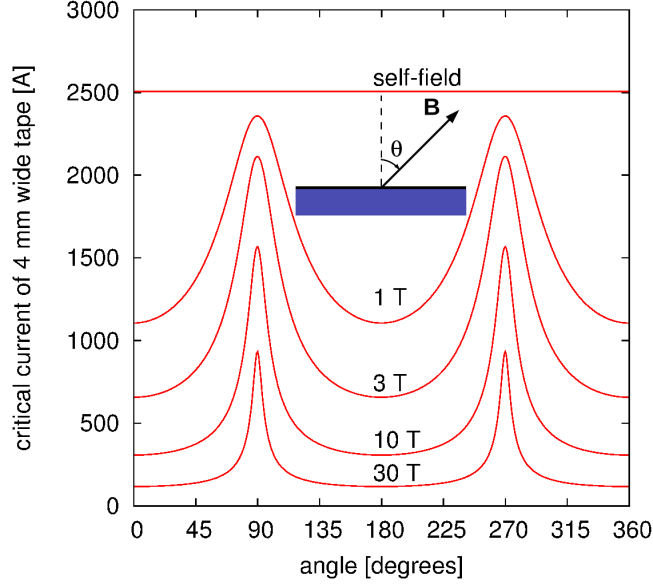


Figure 3: Anisotropic magnetic field dependence of the tape critical current, $I_{ct}(B, \theta)$, as input for the calculations, given by equations (2) and (3) [29]. We assume that the local J_c follows $J_c = I_{ct}/(wd)$, where w and d are the width and thickness of the superconducting layer, respectively.

algorithm sets uniform ΔJ in the tape cross-section, $\Delta J = \Delta I/(wd)$. Then, the vector potential ΔA due to ΔJ and the magnetic field \mathbf{B} are calculated in all elements in each sector but taking only the contribution from ΔJ outside the considered sector. We name these quantities as ΔA_e and \mathbf{B}_e . Afterwards, the routine obtains J at each sector ignoring the magnetic interaction with all the other sectors and taking ΔA_e and \mathbf{B}_e as applied fields. The algorithm iterates until the maximum difference between iterations is below a certain tolerance. In order to ensure convergence of the iterative process, we apply a damping factor $0 < k < 1$ such that $\Delta J := k\Delta J + (1-k)\Delta J_p$, where ΔJ_p is ΔJ at the previous iteration. The whole process is repeated for subsequent time increases Δt until the desired final time is reached, obtaining the whole time evolution. At the beginning of the time evolution we take $t_0 = 0$, $I_0 = 0$ and we assume $J_0 = 0$, corresponding to the zero-field cool situation. The effect of the magnetic field generated by an external winding, such as a low-temperature superconducting outsert, can be simply taken into account by adding its contribution to ΔA_e and \mathbf{B}_e .

For coils with many turns, this method greatly reduces the computing time. Since the computing time scales with the number of turns N as N^α with $\alpha = 2$ (figure 6); for a large number of turns, solving m problems of N/m turns takes only $1/m^{\alpha-1}$ of the original computing time. The number of iterations is kept low because the Screening Current Induced Field (SCIF) that the sector creates has a range of the order of the tape width, which corresponds to the sector size. In addition, this method can be easily parallelized, using up to as many tasks as sectors. The routine in this work uses more than 90 % of the computing power of a 12-core computer for high number of turns. The sub-routine to calculate

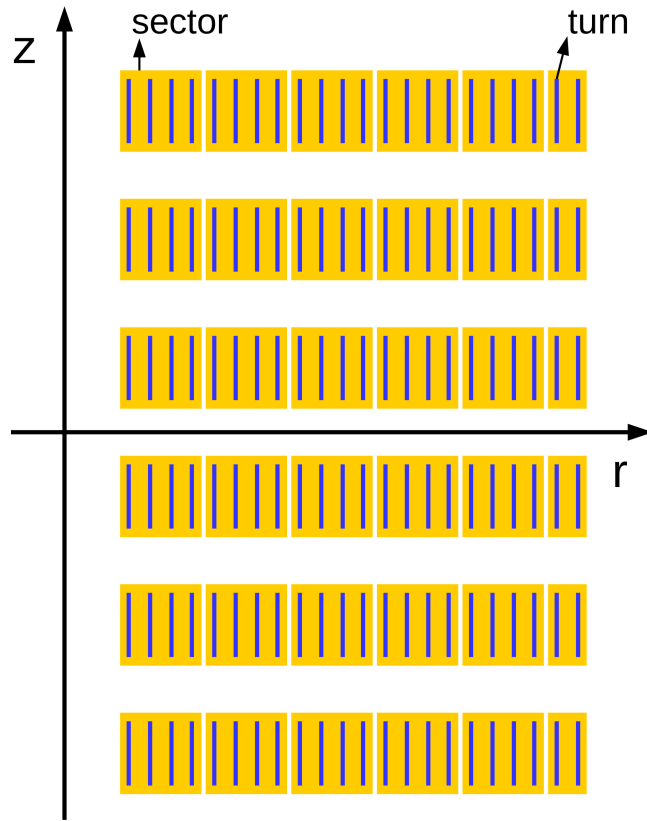


Figure 4: Dividing the coils into sectors enables to speed up the computations and efficiently parallelize the numerical method.

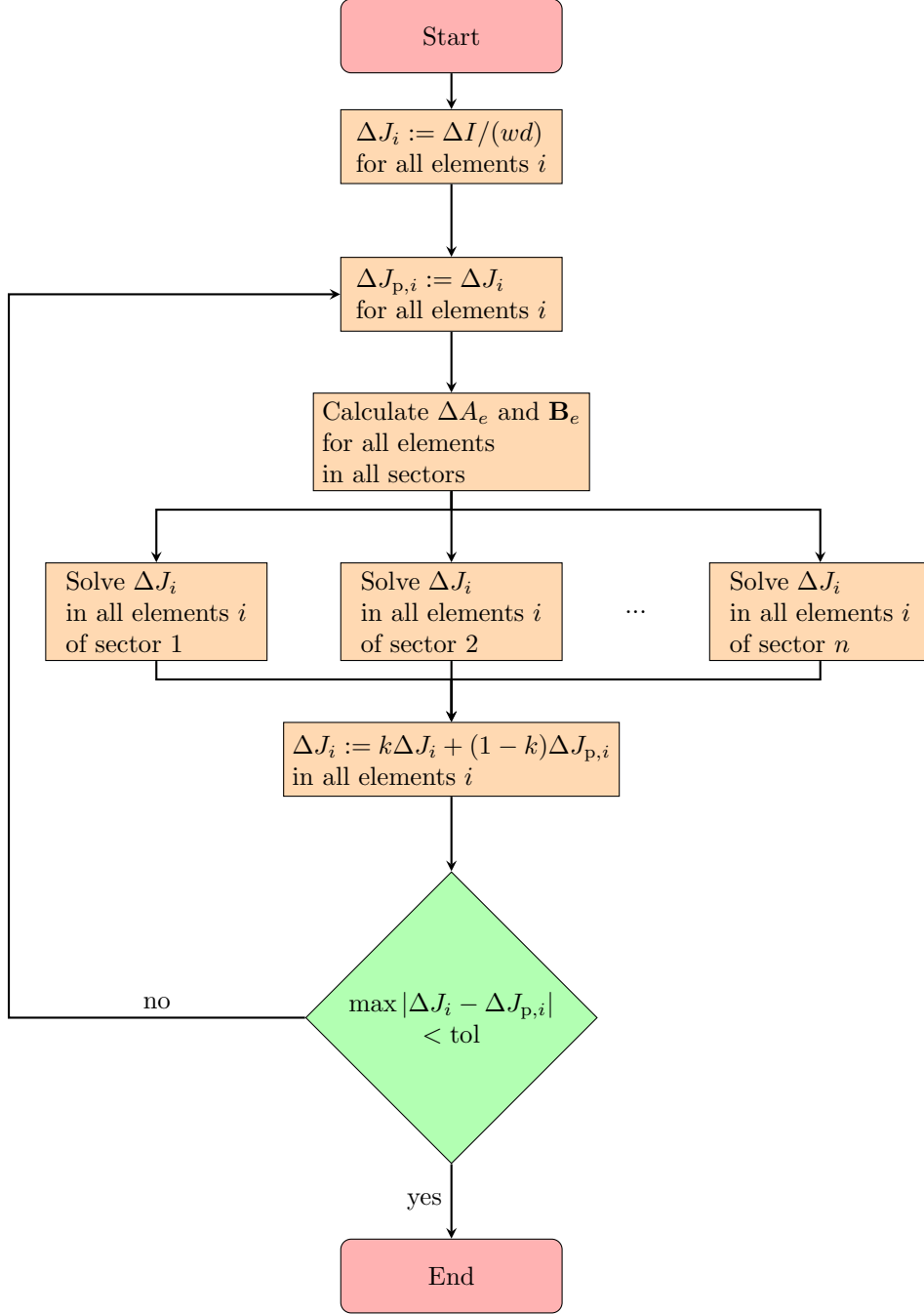


Figure 5: The iterative parallel algorithm rapidly calculates the screening currents without loss of accuracy (simplified version for clarity).

ΔA_e and \mathbf{B}_e is also parallelized.

The computing time can be further reduced by using the continuous approximation for densely packed pancake coils [9, 12, 17]. This results in a reduction of the effective number of turns per pancake, in our case from 400 real turns to 40 effective turns.

Figure 6 shows the computing time for both the real and continuous approximations. The computed case is the time evolution of the first ramp increase from 0 to the coil critical current. These calculations have been done in a computer with two 6-core Intel Xeon E5645 processors, where the required RAM is below 9 Gb for all cases. Computing times are similar to those in a standard 4-core (8 threads) processor Intel Core i7-4770K. Using 50 elements in the superconductor width and one in the thickness, the computing time for the real geometry with 400 and 1000 turns is around 30 min and 4.5 hours, respectively, and the computing time for 10000 turns is around 20 days (figure 6a). Using the continuous approximation greatly reduces the computing time (20 seconds, 103 seconds and 3 hours for 400, 1000 and 10000 turns, respectively), resulting in a factor around 100 reduction for high number of turns. This is consistent with the reduction of the effective turns by a factor 10 and the quadratic scaling of the computing time with the number of elements for high number of elements (figure 6b). The lower slope in figure 6b for the continuous approximation at low number of elements is due to a less efficient parallelization of the routine. With the continuous approximation, calculations for up to 40000 turns and 0.5 million elements in the superconductor have been effectuated in practical computing times. For all calculations, the computing time can be further reduced to half, if the mirror symmetry in the axial direction is assumed.

The DC critical current of a certain turn u is calculated by taking a very slow ramp (10^{-14} A/s). For this case, the general relation $E = -\partial_t A - (1/r)\partial_\varphi \phi_u$ becomes $E \approx -(1/r)\partial_\varphi \phi_u$, where ϕ_u is the scalar potential at turn u , r and φ are the radial and angular coordinates, respectively, and $\partial_\varphi \phi$ is uniform⁴. The critical current of turn u is that which follows $E = E_c$ in that turn. We take the critical current of the whole coil as that of the weakest turn. Comparing to other methods [31–33], the method in this article takes the precise magnetization currents into account. In addition, it allows to calculate the coil DC current-voltage curve with non-uniform power-law exponent, n , and $n(B, \theta)$.

4 Results and discussion

This section presents the results for the screening currents, Screening Current Induced Field (SCIF) and instantaneous AC loss for the coil with parameters in table 1. The SCIF at the remnant state and the critical current is also presented for coils from 2 to 100 pancakes. The number of elements per turn (real or effective) is between 50 and 200, being the higher number of elements for the loss computations. The ramp rate is for 2 A/s for figures 7,8,9,11 and 0.2 A/s for the rest, being the qualitative behavior independent on this parameter.

⁴For axial symmetry, $\mathbf{E} = E(r, z)\mathbf{e}_\varphi$, where \mathbf{e}_φ is the unit vector in the angular direction. Thus, $\mathbf{E} = -\partial_t \mathbf{A} - \nabla \phi$ implies $\partial_r \phi = \partial_z \phi = 0$, and hence $\phi(r, \varphi, z) = \phi(\varphi)$. Since $E(r, z)$ does not depend on φ , $\partial_\varphi \phi$ is constant.

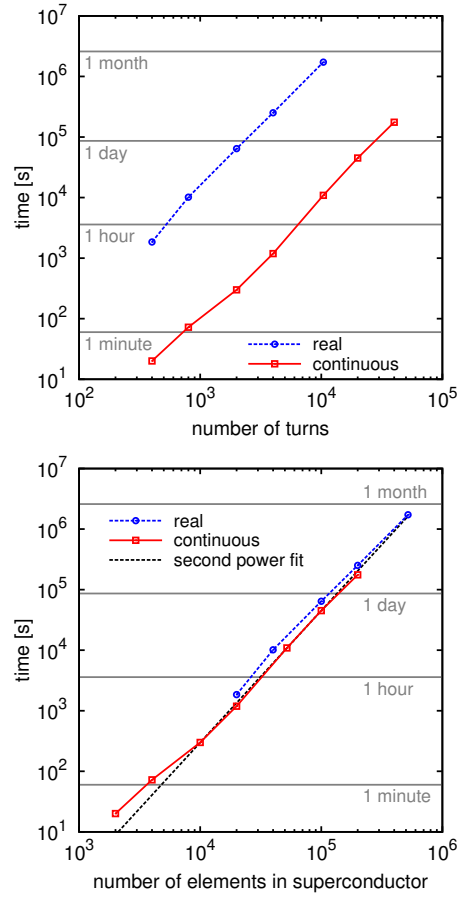


Figure 6: The self-programmed modeling tool computes coils up to 10400 turns for the real geometry and 40000 turns for the continuous approximation in feasible computing times, which scales as the second power of the number of turns or the number of elements.

4.1 Current density

Figure 7 shows the current density at the peak of the charge cycle in the coil of 400×26 turns for the detailed model (coil cross-section in figure 1 and current signal in figure 2). For this case, we assumed a power-law exponent of 30. The computed situation is for a peak current of 226 A, which represents 76 % of the critical current. A zoom of the area marked by a black frame is in figure 8, showing the individual turns. The largest screening currents are at around $3/4$ of the coil height (6th and 7th pancakes from the top). This is because at the end turns the large magnetic field, around 8 T, substantially suppresses J_c ; at the central turns, the radial field is much lower than the penetration field of the pancake, and hence screening currents are small. The screening currents are roughly the same in all turns of each pancake, except at the 8-10 turns the closest to the inner and outer radius (see figure 8). At the 3 pancakes the closest to the end, variations of the screening currents in the radial direction are due to variations in the magnetic field, specially its radial component.

The continuous approximation reproduces the same current density as the real geometry (see figures 7 and 9), except of a certain averaging in the radial direction for the 8-10 turns the closest to the inner or outer radius. The results could be improved by using thinner effective turns close to the inner and outer radius.

The magnitude and current penetration process can be better appreciated in the line plots of the current density at the mid radius, 77.95 mm (see figures 10 and 12 for the continuous approximation).

The typical penetration process of the initial ramp can be seen from pancake 3 from the coil end in figure 10a. First, the current penetrates with $|J| \approx J_c$ (critical region) from both sides with a sub-critical region in between (profile 11). The magnetic field dependence of J_c causes a variation of J_c in the axial direction. The radial field vanishes at the sub-critical region (region with $|J|$ substantially smaller than J_c), and hence $|J|$ is the largest at the front of critical current density. The current does not vanish in the sub-critical region. By further increasing the current I , the critical region expands until it fully penetrates the tape (profile 12). Afterwards, J_c decreases due to the increase of B_r and the zone with negative current is reduced, caused by the increase of I (profile 13).

For the decreasing ramp, we also analyze pancake 3 from the coil end in figure 10b. A zone with $|J| \approx J_c$ is created (reverse critical region) with J of the opposite sign from the preexisting (profile 14). The penetration process continues until the sample saturates, while the current density increases in the reverse critical region (profile 15); this is caused by the increase of J_c due to the decrease of the radial magnetic field. After full penetration, J further increases (profile 16). An example of partial penetration of the reverse critical region is pancake 6 from the end, where there remains a zone with J induced at the initial ramp enclosed by the reverse critical region.

At the remnant situation, or end of the discharge ramp, screening currents are more important than at the maximum current (figures 11 and 10b). The reasons are the following: first, the transport current in the charge curve partially depletes the region of negative current; second, the radial field for the remnant case is reduced down to the self-field of the pancake (≈ 3 T at the center of the top pancake, compared to ≈ 8 T), resulting in higher J_c . The maximum

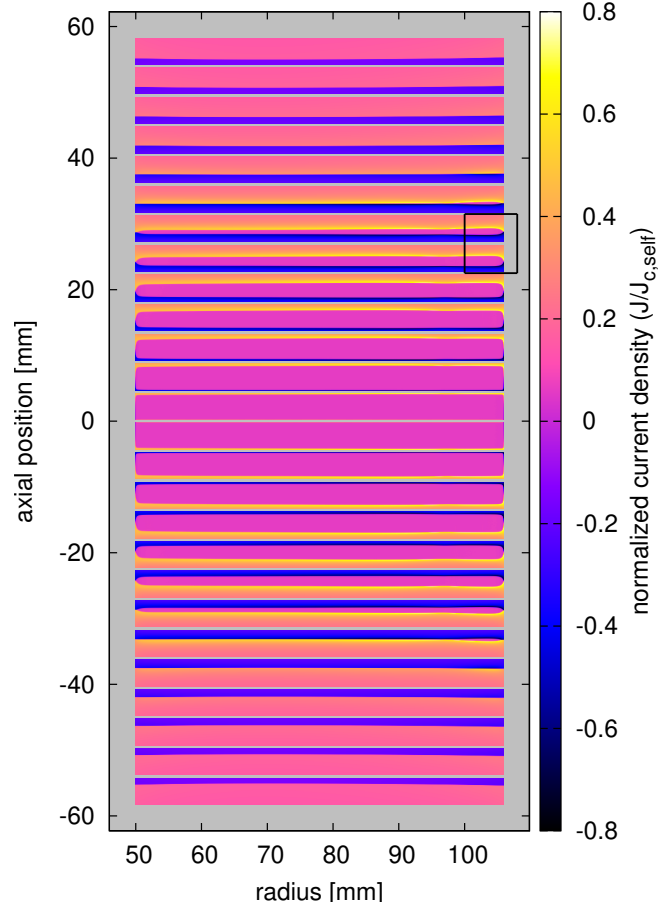


Figure 7: The coil presents important screening currents at the end of the (first) increasing ramp. Results are for the real geometry; the pancakes cross-section is depicted as continuous for clarity. A detail of the region within the black frame is shown in figure 8.

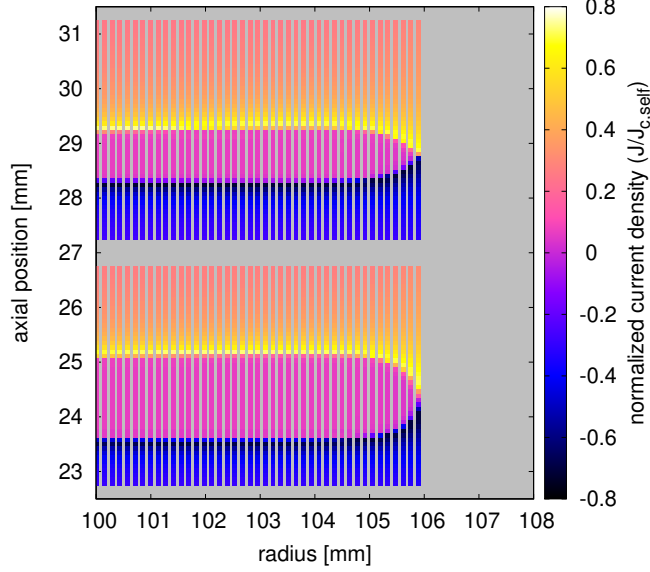


Figure 8: Detail of the screening currents in figure 7 (area within the black frame there). The superconducting-layer thickness is expanded in the plot for visibility (computations use realistic $2 \mu\text{m}$ thickness).

screening currents are at the top 4 pancakes, since there the variation of radial field from the peak current is the largest.

If the current is switched off at the remnant state, the average current density decreases due to relaxation caused by the finite power-law exponent. For our case, relaxation after 10^7 seconds appreciably reduces the screening currents, although they are still important (figure 12).

4.2 Screening Current Induced Field

In the following, we analyze the SCIF at the bore center. We consider the 10400 turns coil of table 1 for both cyclic ramp-up and ramp-down excitations (section 4.2.1) and relaxation of the remnant state (section 4.2.2). Section 4.2.3 describes the effect of the number of pancakes, or coil size, on the SCIF at the remnant state.

4.2.1 Cyclic charge and discharge

For the initial ramp, taking the continuous approximation into account reproduces the curve for the real situation with a maximum deviation of 0.2 % of the SCIF at the peak, as shown in figure 13. Then, the continuous approximation can be used to predict the SCIF and optimize the magnet design regarding this aspect.

For the cyclic charge and discharge (figure 2b), the SCIF at the first charge is different than that at the following charges (see figure 13) due to the residual current density from the previous discharge. The magnitude of the SCIF slowly decreases with the number of charges until it reaches a steady-state cycle (see

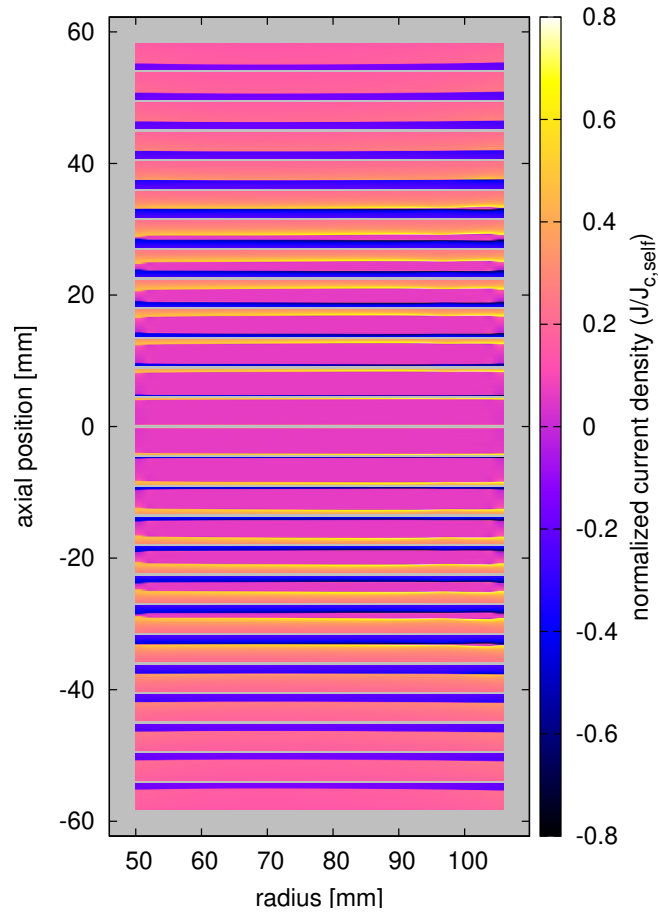


Figure 9: The screening currents for the continuous approximation agree with those for the real geometry (same situation as figure 7).

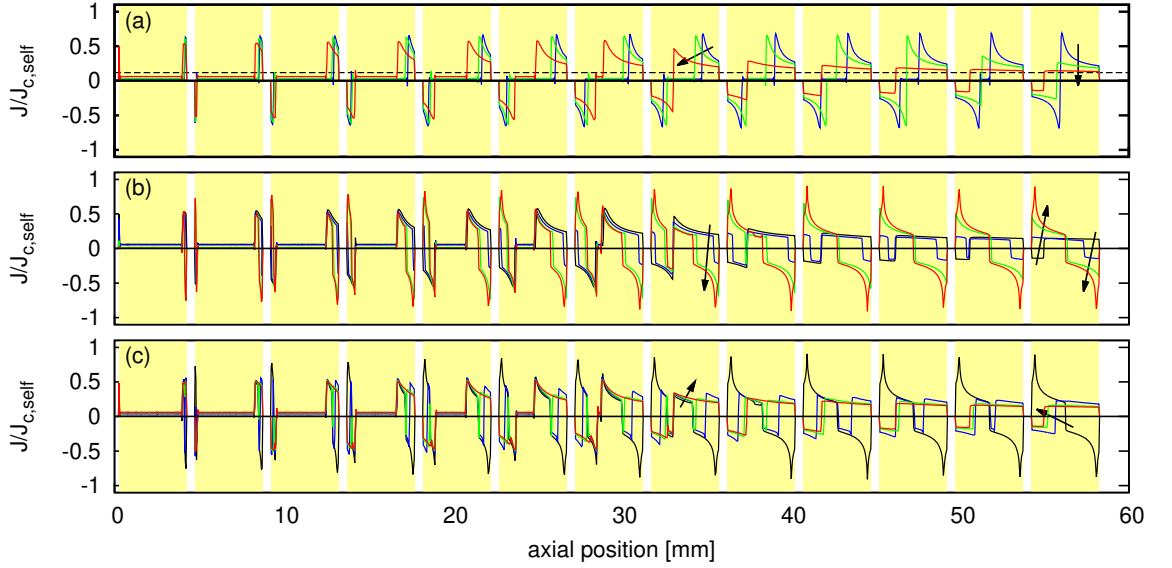


Figure 10: The current density in the turns at the mid radius show the main features of the current penetration process (continuous approximation). The situation for each curve corresponds to those in figure 16a with labels 11,12,13 (a), 13,14,15,16 (b), and 16,17,18,19 (c) in the arrows direction. The horizontal dash line in (a) represents the current density at the end of the ramp if magnetization currents are not present.

inset of figure 13). This is caused by the finite power-law exponent of the $E(J)$ relation, which allows relaxation of the residual screening currents created at the first charge. At the initial charge, the decrease of the SCIF with increasing the current at high currents is due to both a depletion of negative current caused by transport current and the suppression of J_c as a consequence of the increase of the magnetic field.

The SCIF in the coil of figure 1 is relatively large compared to the maximum generated field (the SCIF are -0.37 T and 0.61 T at the peak and remnant state, respectively, compared to 14.9 T generated magnetic field at the peak). This may be an issue for applications that require generated magnetic fields of high quality (homogeneity and stability), such as MRI or NMR.

4.2.2 Relaxation in remnant state

After one single charge and discharge (case in figure 2a), the SCIF decreases with time due to the smooth $E(J)$ relation (see figure 14). At high relaxation times, the SCIF decreases exponentially, which is a typical behavior for power-law $E(J)$ relations [34]. The change in the SCIF is 19, 65, 101, 122, 138 mT in 1 minute, 1 hour, 1 day, 1 week and 1 month, respectively, representing 0.13, 0.44, 0.68, 0.82, 0.93 % of the generated magnetic field at the peak of the current.

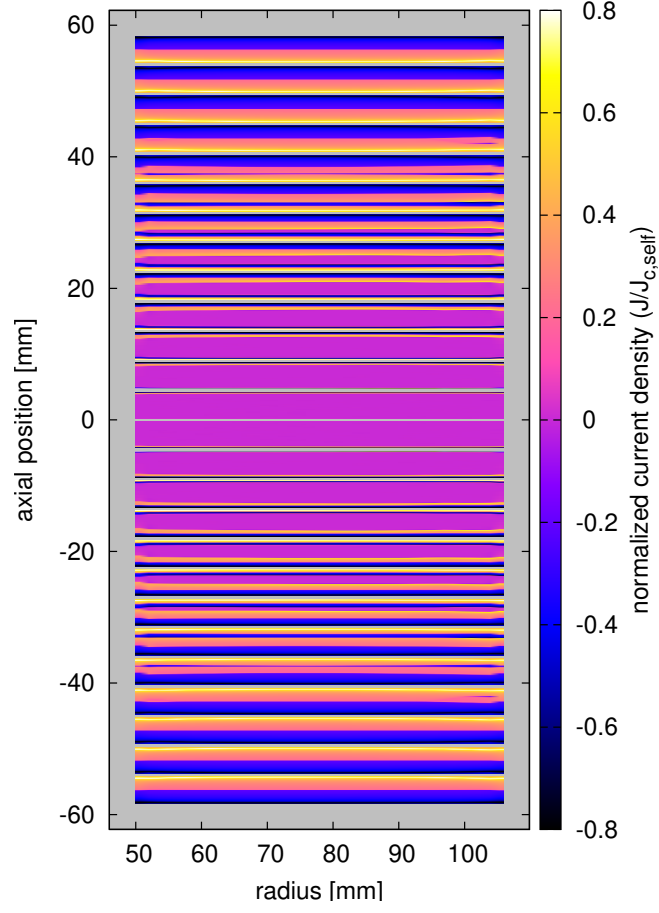


Figure 11: The screening currents are the most important at the remnant state (results for the continuous approximation).

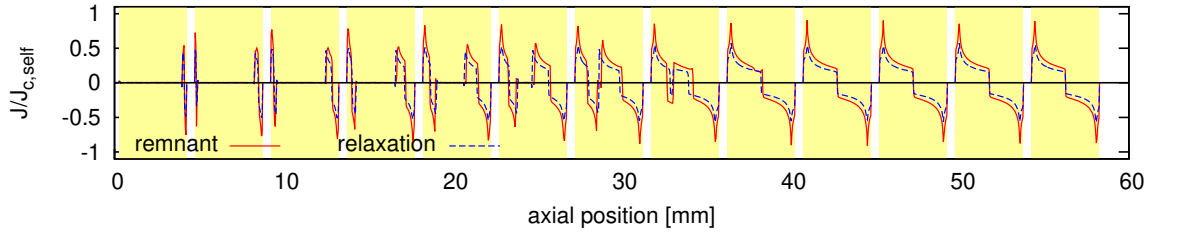


Figure 12: Relaxation after the remnant state (situation of figure 2b) reduces the screening currents (results for the turns at the mid radius for the continuous approximation).

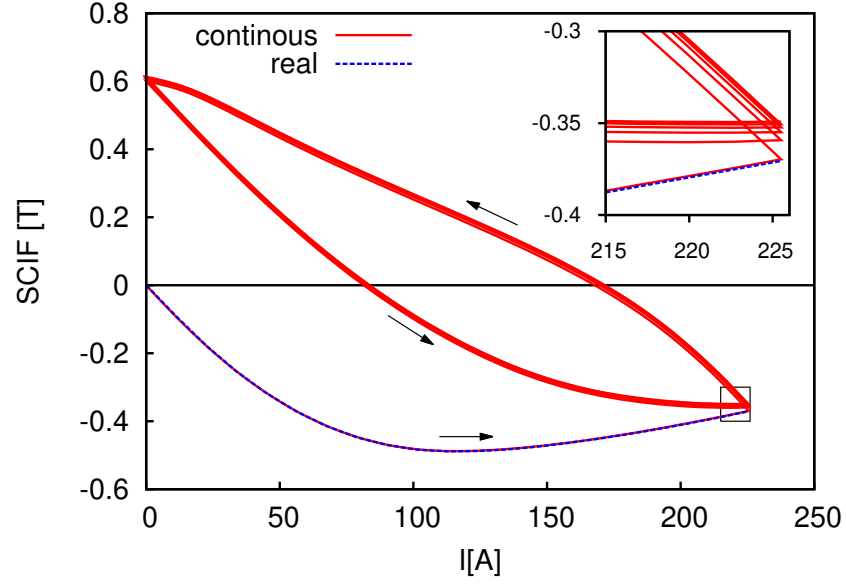


Figure 13: The screening current induced field (SCIF) taking the real geometry and continuous approximation agree with each other. The inset shows a detail of the area within the black frame.

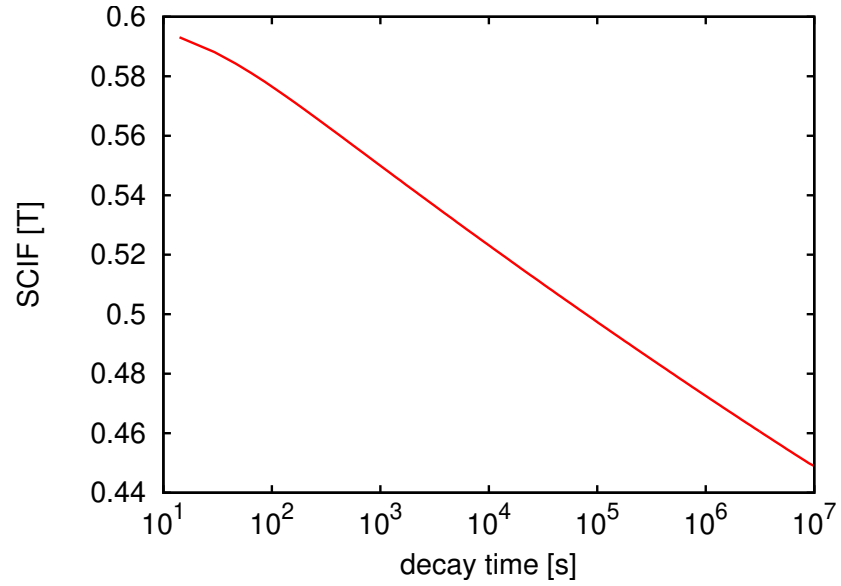


Figure 14: The Screening Current Induced Field (SCIF) decays in time roughly exponentially.

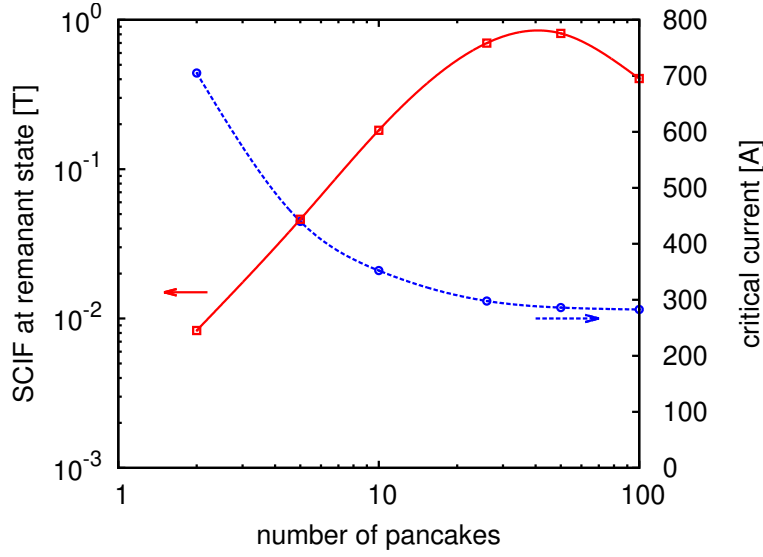


Figure 15: The Screening Current Induced Field (SCIF) at the remnant state presents a peak with increasing the number of pancakes, while the critical current saturates.

4.2.3 Dependence on the number of pancakes

To study the dependence of the SCIF on the coil size, we calculated the SCIF at the remnant state for coils from 2 to 100 pancakes, where each pancake contains 400 turns (40000 turns in total for the largest coil). For all coils, we considered the case that the peak current corresponds to the coil critical current.

The critical current decreases with the number of pancakes until it saturates for a high number of pancakes (see figure 15; data in table 2). For all cases, the turn limiting the critical current is located at the top pancake. This behaviour is caused by the fact that J_c is very sensitive to the radial field and this is the highest at the top pancakes. With increasing the number of pancakes, the radial field increases until it saturates for long coils. The position of the maximum radial field at the top pancake moves to inner radius with increasing the number of pancakes. As a consequence, the turn with the lowest critical current at the top pancake moves accordingly (table 2).

The SCIF at the coil center increases with the number of pancakes until around 40 pancakes and then it decreases for higher number of pancakes (see figure 15). The reason is that for high number of pancakes, the height-over-width aspect ratio of the winding is large. For this geometry, the radial magnetic field is low except at the coil ends. As a consequence, the screening currents are only important close to the coil ends. Then, with increasing the coil height, the distance between the pancakes contributing to the SCIF and the coil center increases, and hence the SCIF decreases.

4.3 AC loss

In order to understand the causes of the time dependence of the power AC loss, we calculated both the same situation as figure 13 (anisotropic magnetic-field

number of pancakes	number of turns	turn with lowest critical current	critical current [A]
2	800	310	705
5	2000	150	440
10	4000	140	352
26	10400	130	298
50	20000	130	286
100	40000	130	283

Table 2: Critical current of the weakest turn for coils with several number of pancakes (the rest of the parameters are the same as those in table 1). The turn with the lowest critical current is always at the end pancakes.

dependence of J_c from equations (2) and (3) and power-law exponent 30) and that for constant J_c and power-law exponent 1000, the latter corresponding to the Bean’s critical state model. For the Bean’s situation, we took $J_c = I_c/(wd)$, where I_c is the coil critical current for the magnetic-field dependent J_c . Although the loss per cycle is of the same order of magnitude (7.72 and 6.81 kJ for the Bean’s and $J_c(B, \theta)$ cases, respectively), the instantaneous loss differs substantially and presents different qualitative behavior for the ramp decreases (figure 16).

4.3.1 Bean’s case

For the Bean’s case, the loss at the initial ramp increases as I^2 until it reaches an inflexion point (point 1 in figure 16). The I^2 dependence is explained by the partial penetration by J_c , as has been shown for slabs in applied magnetic field [35]. The inflexion point corresponds to the penetration of the the two pancakes from the top (figure 17a profile 1). Afterwards, the loss increases slower with roughly a linear dependence. This linear dependence roughly starts when the top six pancakes are fully penetrated (figure 17a profile 2), which generate most of the AC loss. Again, the I dependence is consistent with the behavior of a fully penetrated slab under applied magnetic field. For large enough current, the loss rises faster than a liner dependence due to the direct effect of the transport current, which creates dissipation due to dynamic magneto-resistance.

At the beginning of the ramp decrease, the loss drops, since the time derivative of the current vanishes (figure 16). Later, when the critical region with reverse current density meets the sub-critical region (figure 17b profile 5), the loss experience a sharp increase (point 5 in figure 16). This is because a small change in I causes penetration of the sub-critical region, becoming exposed to the magnetic flux “external” to the pancake, and hence that region also experiences AC loss. This penetration of the sub-critical region is slower for pancakes further from the ends, since the increase of the “external” magnetic field is smaller for the same current increase. Therefore, when a sufficient amount of pancakes are penetrated, the loss starts to decrease (figure 16). At a certain time, the loss increases again because by decreasing I , the magnetization currents at the fully penetrated pancakes increase; since by decreasing I , the current constrain allows a higher volume for the magnetization currents (compare profiles 6 and

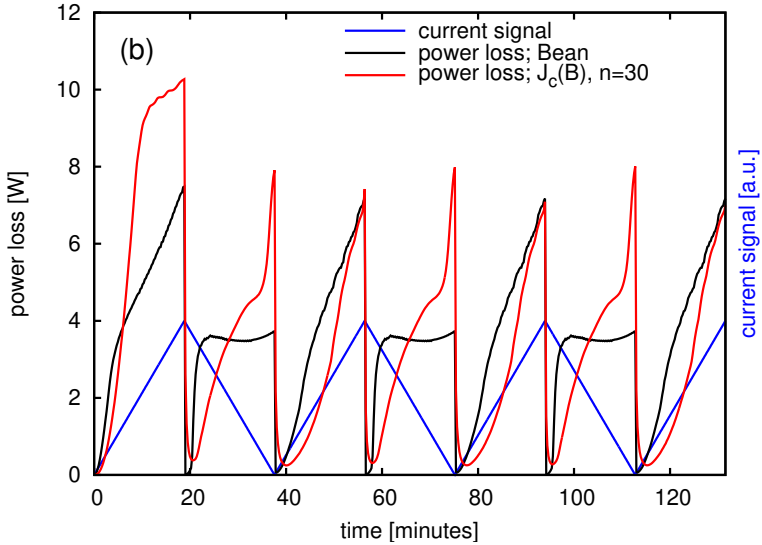


Figure 16: The instantaneous AC loss for the taken $J_c(B, \theta)$ dependence and power-law exponent $n = 30$ is qualitatively very different than that for constant J_c and $n = 1000$ (critical-state model or “Bean” case). The numbers in (a) represent the key events in the current penetration process (see figures 10,17 and text). The peak current is $I_m=226$ A.

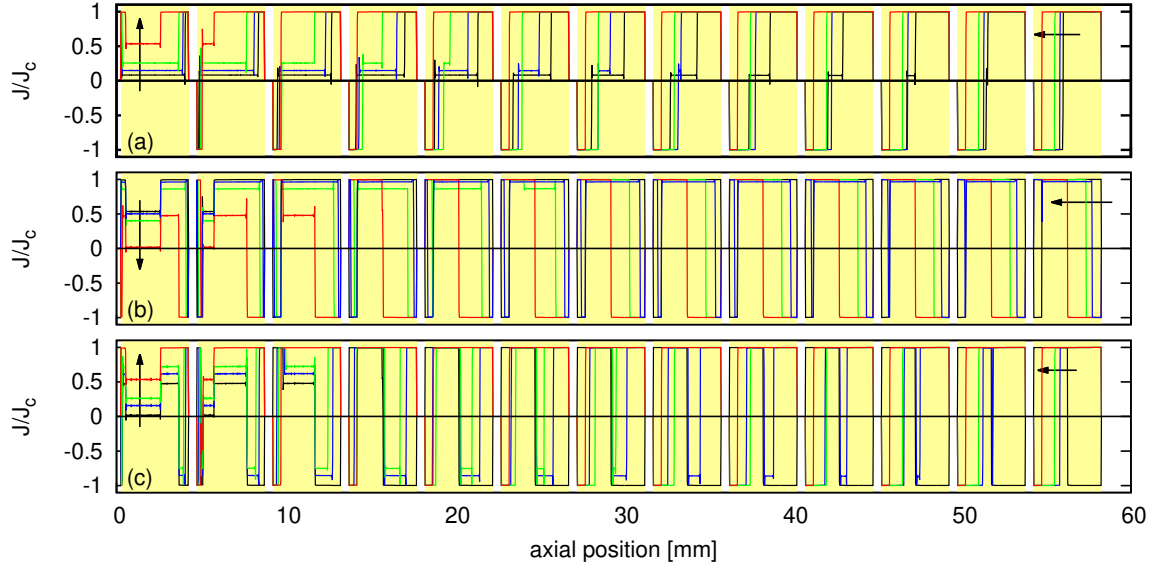


Figure 17: Current density in the turns with mid radius for constant J_c and power-law exponent 1000, corresponding to the critical-state model. The situation for each curve is the same as that of the points in figure 16a with labels 1,2,3,4 (a), 4,5,6,7 (b), 7,8,9,10 (c), following the arrow direction.

7 in figure 17b for the 7 upper pancakes).

At the second ramp increase, the qualitative behavior is the same as for the initial curve (figure 16). The only difference is that the quadratic dependence, appearing during partial penetration of the newly created critical region, expands to higher I (up to point 8 in figure 16). That is because for this case the local change in J during critical zone penetration is $2J_c$, instead of only J_c in the initial curve (figures 17a and 17b).

4.3.2 Anisotropic magnetic field dependence of J_c

For the $J_c(B, \theta)$ dependence, the initial curve is qualitatively the same as for the Bean's case (figure 16). However, the interval with quadratic increase is larger (interval up to point 11). The quasi-linear increase that follows presents a lower slope because J_c decreases with increasing I due to the increase of the radial magnetic field. The loss at the current peak is higher for $J_c(B, \theta)$ because the local J_c is higher in the pancakes 2 to 7 from the end, producing higher magnetization loss.

The loss in the decreasing ramp looks very different from the Bean's case (figure 16). Although it also starts with an increase after the penetration of the first pancake (point 14 in figure 16 and profile 14 in figure 10b), this increase presents a lower rate because when decreasing I , the decrease of B_r causes an increase of J_c of the reverse critical region. As a consequence, penetrating subsequent pancakes requires a larger variation of I (or magnetic field), due to the larger shielding capability of the reverse currents. Between points 15 and 16 in figure 16, there is a sharp increase of the loss. In this interval, there is practically no further penetration by reverse current but the current density at

the fully penetrated pancakes sharply increases due to the decrease of the local B and the sharp $J_c(B)$ dependence at low B (current profiles in 10b).

The loss in the second ramp increase is qualitatively similar to the first ramp, except that the region with quadratic increase expands to a much larger interval for the same reasons as for the Bean's case. The loss at the end of the second ramp increase is lower than at the end of the first. The cause is that at the end of the second ramp, the newly induced critical region, where E is significant, is smaller than that in the initial curve [except for the five pancakes from the top, where J is the same (figures 10a and 10c)]. In the other pancakes, the small deep in $|J|$ in the negative J region shows the border between both critical regions (profile 19 of figure 10c). For ramp increases after the first, the loss at the peak slightly decreases with the number of cycles. The reason is the decay of the frozen current density at the first ramp, caused by the finite power-law exponent. This also causes a time delay of the loss minimum at the end of all ramps.

5 Conclusions

This article presented detailed modelling of the screening currents and the screening current induced field (SCIF) of coils with more than 10000 turns for the real geometry and 40000 turns for the continuous approximation. We also analyzed the instantaneous power loss and the causes that create it. Since we used an anisotropic field dependence of J_c extracted from measurements at 4.2 K from self-field up to 30 T, the results are representative for high-field magnets. The qualitative behavior is valid for any winding containing densely packed pancake coils, such as SMES.

The calculations used the MEMEP numerical method [18]. In order to achieve feasible computing times while keeping the same accuracy, we developed a fast iterative routine that we efficiently parallelized. The same concept might be applied to conventional finite-element methods (FEM).

The results show that the continuous approximation is suitable to calculate the screening currents and the SCIF, while further reducing the computing time. For a cyclic charge and discharge process, the stationary loop is achieved after several cycles due to the assumed power-law $E(J)$ relation, which causes relaxation of the magnetization currents induced at the first ramp. With increasing the number of pancake coils, the SCIF at the remnant state presents a peak at around 40 pancakes, while the coil critical current monotonically decreases until it saturates. Comparing to the results with a realistic $J_c(B, \theta)$, taking J_c from the coil critical current results in a loss per cycle of the same order of magnitude (only 13 % overestimation) but the instantaneous loss is very different. Saturation of the magnetization currents at the end pancakes, where the AC loss is the largest, causes that the maximum AC loss at the first ramp increases with increasing the critical current density.

This article have shown that the presented model can accurately calculate the SCIF in practical computing times for coils with any number of turns used in real windings. Such modeling could also predict the power loss in the charge and discharge process and the relaxation of the SCIF after one charge or discharge cycle. Experimental data on the anisotropic magnetic field dependence of the power-law exponent may be used to refine the calculations.

Acknowledgements

The research leading to these results has received funding from the European Union Seventh Framework Programme [FP7/2007-2013] (grant NMP-LA-2012-280432) and the Structural Funds of EU (grant ITMS 26240220088)(0.5). The authors acknowledge the use of resources provided by the SIVVP project (ERDF, ITMS 26230120002).

References

- [1] F. Grilli, E. Pardo, A. Stenvall, D. N. Nguyen, W. Yuan, and F. Gömöry. Computation of losses in HTS under the action of varying magnetic fields and currents. *IEEE Trans. Appl. Supercond.*, 24(1):8200433, 2014.
- [2] H. Maeda and Y. Yanagisawa. Recent developments in high-temperature superconducting magnet technology (review). *IEEE Trans. Appl. Supercond.*, 24(3):4602412, 2014.
- [3] H. W. Weijers, W. D. Markiewicz, A. J. Voran, S. R. Gundlach, W. R. Sheppard, B. J. Jarvis, Z. L. Johnson, P. D. Noyes, J. Lu, H. Kandel, et al. Progress in the development of a superconducting 32 T magnet with REBCO high field coils. *IEEE Trans. Appl. Supercond.*, 24(3):4301805, 2014.
- [4] Q. Wang, J. Liu, S. Song, G. Zhu, Y. Li, X. Hu, and L. Yan. High temperature superconducting ybco insert for 25 T full superconducting magnet. *IEEE Trans. Appl. Supercond.*, 25(3):1–5, 2015.
- [5] S. Awaji, K. Watanabe, H. Oguro, S. Hanai, H. Miyazaki, M. Takahashi, S. Ioka, S. Fujita, M. Daibo, Y. Iijima, et al. New 25 T cryogen-free superconducting magnet project at Tohoku university. *IEEE Trans. Appl. Supercond.*, 24(3):4302005, 2014.
- [6] Y. Mawatari. Critical state of periodically arranged superconducting-strip lines in perpendicular fields. *Phys. Rev. B*, 54(18):13215, 1996.
- [7] E. Pardo, A. Sanchez, and C. Navau. Magnetic properties of arrays of superconducting strips in a perpendicular field. *Phys. Rev. B*, 67(10):104517, 2003.
- [8] F. Grilli, S. P. Ashworth, and S. Stavrev. Magnetization ac losses of stacks of YBCO coated conductors. *Physica C*, 434:185–190, 2006.
- [9] E. Pardo. Calculation of AC loss in coated conductor coils with a large number of turns. *Supercond. Sci. Technol.*, 26(10):105017, 2013.
- [10] J. Lu, H. Bai, H.V. Gavrilin, G. Zhang, W.D. Markiewicz, and H.W. Weijers. AC losses of ReBCO pancake coils measured by a calorimetric method. *IEEE Trans. Appl. Supercond.*, 25(3):1–5, 2015.
- [11] E. Pardo. Modeling of coated conductor pancake coils with a large number of turns. *Supercond. Sci. Technol.*, 21:065014, 2008.

- [12] L. Prigozhin and V. Sokolovsky. Computing AC losses in stacks of high-temperature superconducting tapes. *Supercond. Sci. Technol.*, 24:075012, 2011.
- [13] VM Rodriguez-Zermeno, N. Mijatovic, C. Traeholt, T. Zirngibl, E. Seiler, AB Abrahamsen, NF Pedersen, and MP Sorensen. Towards faster FEM simulation of thin film superconductors: A multiscale approach. *IEEE Trans. Appl. Supercond.*, 21(3):3273–3276, 2011.
- [14] M.D. Ainslie, T.J. Flack, and A.M. Campbell. Calculating transport AC losses in stacks of high temperature superconductor coated conductors with magnetic substrates using FEM. *Physica C*, pages 50–56, 2012.
- [15] E. Pardo, J. Šouc, and J. Kováč. AC loss in ReBCO pancake coils and stacks of them: modelling and measurement. *Supercond. Sci. Technol.*, 25:035003, 2012.
- [16] M. Zhang, W. Yuan, D. K. Hilton, M. D. Canassy, and U. P. Trociewitz. Study of second-generation high-temperature superconducting magnets: the self-field screening effect. *Supercond. Sci. Technol.*, 27(9):095010, 2014.
- [17] V. M. R. Zermeno, A. B. Abrahamsen, N. Mijatovic, B. B. Jensen, and M. P. Sørensen. Calculation of alternating current losses in stacks and coils made of second generation high temperature superconducting tapes for large scale applications. *J. Appl. Phys.*, 114(17):173901, 2013.
- [18] E. Pardo, J. Šouc, and L. Frolek. Electromagnetic modelling of superconductors with a smooth current-voltage relation: variational principle and coils from a few turns to large magnets. *Supercond. Sci. Technol.*, 28:044003, 2015.
- [19] J. Xia, H. Bai, J. Lu, A.V. Gavrilin, Y. Zhou, and H.W. Weijers. Electromagnetic modeling of REBCO high field coils by the H-formulation. 28(12):125004, 2015.
- [20] L. Quéval, V.M.R. Zermeno, and F. Grilli. Numerical models for ac loss calculation in large-scale applications of HTS coated conductors. *Supercond. Sci. Technol.*, 29(2):024007, 2016.
- [21] N. Amemiya, Y. Sogabe, M. Sakashita, Y. Iwata, K. Noda, T. Ogitsu, Y. Ishii, and T. Kurusu. Magnetisation and field quality of a cosine-theta dipole magnet wound with coated conductors for rotating gantry for hadron cancer therapy. *Supercond. Sci. Technol.*, 29(2):024006, 2016.
- [22] J.R. Clem, J.H. Claassen, and Y. Mawatari. AC losses in a finite Z stack using an anisotropic homogeneous-medium approximation. *Supercond. Sci. Technol.*, 20:1130, 2007.
- [23] W. Yuan, A. M. Campbell, and T. A. Coombs. ac losses and field and current density distribution during a full cycle of a stack of superconducting tapes. *J. Appl. Phys.*, 107:093909, 2010.
- [24] K. Kajikawa, S. Awaji, and K. Watanabe. Numerical evaluation of AC losses in an HTS insert coil for high field magnet during its energization. 2014. arXiv:1405.7765.

- [25] H. Ueda, A. Ishiyama, Y. Ariya, T. Wang, X. Wang, K. Agatsuma, H. Miyazaki, T. Tosaka, S. Nomura, T. Kurusu, S. Urayama, and H. Fukuyama. Evaluation of magnetic-field distribution by screening current in multiple REBCO coils. *IEEE Trans. Appl. Supercond.*, 25(3):1–5, 2015.
- [26] E. Pardo, J. Šouc, and J. Kováč. Relaxation effects and ac loss in superconducting windings: fast parallel numerical model. *4th International Workshop on Numerical Modelling of High Temperature Superconductors*, 2014. Available at www.elu.sav.sk/htsmod2014/Pardo.pdf.
- [27] E. Pardo, J. Šouc, M. Solovyov, L. Frolek, and F. Gömöry. Magnetization currents and AC loss in coated conductor coils of the 10000 turn class: circular magnets and SMES. *International Conference on Magnet Technology 24*, 2015. Presentation number 2OrAA.06.
- [28] M. Kapolka, E. Pardo, J. Kováč, J. Šouc, F. Grilli, R. Nast, E. Demencík, and A. Piqué. 3D modeling and measurement of coupling AC loss in soldered tapes and striated coated conductors. *12th European Conference on Applied Superconductivity*, 2015. Presentation number 3A-LS-O1.8. Available at snf.ieeecsc.org/file/6056/download?token=qAk3YNJy.
- [29] D.K. Hilton, A.V. Gavrilin, and U.P. Trociewitz. Practical fit functions for transport critical current versus field magnitude and angle data from (RE)BCO coated conductors at fixed low temperatures and in high magnetic fields. *Supercond. Sci. Technol.*, 28(7):074002, 2015.
- [30] SuperPower, Inc. <http://www.superpower-inc.com/>.
- [31] J. Pitel. Differences between two definitions of the critical current of HTS coils. *Supercond. Sci. Technol.*, 26(12):125002, 2013.
- [32] F. Gömöry, J. Šouc, E. Pardo, E. Seiler, M. Soloviov, L. Frolek, M. Skarba, P. Konopka, M. Pekarčíková, and J. Janovec. AC loss in pancake coil made from 12 mm wide REBCO tape. *IEEE Trans. Appl. Supercond.*, 23(3):5900406, 2013.
- [33] V. Zermeno, F. Sirois, M. Takayasu, M. Vojenciak, A. Kario, and F. Grilli. A self-consistent model for estimating the critical current of superconducting devices. *Supercond. Sci. Technol.*, 28(8):085004, 2015.
- [34] E. H. Brandt. The flux-line lattice in superconductors. *Rep. Prog. Phys.*, 58:1465–1594, 1995.
- [35] N. Schwerg. Estimation of the instantaneously dissipated hysteresis losses in superconductors. *IEEE Trans. Appl. Supercond.*, 22(4):8200209, 2012.